Materials Today Bio 30 (2025) 101454

Contents lists available at ScienceDirect

Materials Today Bio

journal homepage: www.journals.elsevier.com/materials-today-bio

3D printing of biological tooth with multiple ordered hierarchical structures

Menglu Zhao [a], Yanan Geng [a], Suna Fan [a], Xiang Yao [a], Jiexin Wang [b], Meifang Zhu [a,**], Yaopeng Zhang [a,*]

[a] State Key Laboratory for Modification of Chemical Fibers and Polymer Materials, College of Materials Science and Engineering, Donghua University, Shanghai, 201620, PR China

[b] State Key Laboratory of Organic-Inorganic Composites, Beijing University of Chemical Technology, Beijing, 100029, PR China

ARTICLE INFO

Keywords:
Magnetic-assisted 3D printing
Hydroxyapatite
Anisotropy architecture
Mechanical properties
Bionic crown

ABSTRACT

Natural teeth fulfill functional demands by their heterogeneity. The composition and hydroxyapatite (HAp) nanostructured orientation of enamel differ from those of dentin. However, mimicking analogous materials still exhibit a significant challenge. Herein, a bottom-up, sequential approach was formulated by combining shear-induced and magnetic-assisted 3D printing technology, enabling the fabrication of the intricate microstructure of a multi-material dental crown, where the HAp nanostructure is highly ordered and almost perpendicular to each other at the dentinoenamel junction (DEJ). The HAp nanorods were first induced to achieve high orientation in each printed line, then formed a plane with a vertical structure of DEJ under the shear force and magnetic field at dentin and enamel, respectively, and finally 3D-printed into a dental crown with bilayered parts exhibiting site-specific composition, texture, and outstanding biocompatibility. This novel approach can be applied to design and fabricate natural tooth crowns, indicating the potential for multi-level and multi-dimensional texture control.

1. Introduction

Enamel and dentin of natural teeth are anisotropic biomaterials [1,2]. Current investigations have revealed that the nanostructures exhibit a nearly perpendicular orientation with respect to each other at the dentinoenamel junction [1,3] and can prevent crack propagation [2]. In our previous work, a biomimetic dental crown incorporating multi-level, precisely structured HAp was built by the shear force of 3D printing [4]. However, since the orientation direction can only follow the extruded direction, the above unique three-dimensional structures of teeth cannot be mimicked. Customized arrangement and distribution of magnetized nanoparticles can be achieved in different regions through a directional magnetic field during 3D printing [5]. Ferrand et al. [6] mimicked the layered structure of dentin and enamel found in natural teeth by consecutively pouring distinct aqueous suspensions intoa intricately porous mold exposed in a revolving magnetic field. Only microstructures of teeth were imitated, and its composition and performance did not match the natural tooth. Jiang et al. [7] successfully fabricated artificial enamel materials with strength or microstructures similar to natural enamel. However, natural teeth have a personalized shape larger than 1 cm, thereby posing additional challenges in preparing biomimetic teeth with specific structures and performance [6].

Currently, the utilization of 3D printing in dentistry covers a wide range which represents a significant advancement, starting from the basic printing of dental models using straightforward materials [8], progressing to the printing of high-performance dental materials [9], and ultimately incorporating active cells [10], antibacterial materials [11], and growth factors [12] for functional printing. However, there has been no printing of the anisotropic, biomimetic structure of the tooth body, nor have different composites been exploited to design enamel and dentin heterogeneity. By utilizing shear forces during the 3D printing process [13,14], external magnetic fields [15–18], or sound waves [19,20], anisotropic whiskers can be oriented in specific directions and positioned accordingly. This approach allows for the control of the structure and functionality of composite material [21,22]. The magnetically induced 3D printing technique, which involves utilizing an

* Corresponding author.
** Corresponding author.zmf@dhu.edu.cn
E-mail address: zyp@dhu.edu.cn (Y. Zhang).

https://doi.org/10.1016/j.mtbio.2025.101454
Received 21 July 2024; Received in revised form 6 November 2024; Accepted 3 January 2025
Available online 3 January 2025

externally oriented magnetic field to align and distribute magnetized nanoparticles, has been employed in various studies. For instance, Kokkinis et al. [15] used a multi-nozzle direct ink writing (DIW) process in combined with magnetically induced orientation of magnetic particles to achieve integrated manufacturing of multi-materials. Ma et al. [17] utilized DIW in conjunction with a magnetic assistance method to realize the fabrication of a novel type of ultra-antiwear flexible sensor. Further research is still needed on magnetically induced 3D printing materials and their applications within the dental field.

In the pursuit of artificial dental restorative materials, researchers have explored various strategies to repair damaged enamel, encompassing but not limited to biomimetic mineralization [23,24], resin-based composite fillings [25,26], and advanced ceramic coating technologies. [27,28] Nevertheless, these approaches still confront challenges in mimicking the complex microstructures, biocompatibility, and long-term durability of natural teeth. Consequently, there is an urgent need to develop artificial teeth that can precisely replicate the multi-layered microstructures of natural teeth while possessing superior mechanical properties and biocompatibility. This endeavor not only aims to enhance patients' quality of life but also alleviates the burden on the dental profession, fostering advancements in dental medicine.

Inspired by the different preferential orientations of nanostructures in enamel and dentin (Fig. 1), we developed a bottom-up, incremental assembly approach utilizing multi-nozzle 3D printing technology, combining shear-induced and magnetically induced ordered structures to prepare a dental crown of utmost precision incorporating an ordered, hierarchical structure of HAp. First, HAp nanorods were magnetized by electrostatic adsorption and sintering of amino-surface-modified HAp nanorods and SPION@SiO_2 core-shell powders. HAp arrangement was precisely controlled by fine-tuning the directions of the printed splines and magnetic field, and a complex dental crown architecture featuring perpendicular nanostructures that are meticulously organized and precisely aligned at DEJ was finally 3D-printed to mimic the anisotropic structure of human teeth. The magnetized HAp-based resin-based composites (RBCs) demonstrated impressive mechanical robustness, despite with minimal concentrations of HAp, making them ideal for fabricating 3D configurations featuring uniformly oriented nanofillers. Based on our current comprehension, the achievement of a 3D-printed perfectly executed crown incorporating anisotropic and ordered architecture derived from HAp nanostructures, remains unprecedented. Our research sets the cornerstone of biomimetic materials advancements that possess distinctive formations and functionalities, showing a crucial role in the field of biomaterials engineering.

2. Results and discussion

2.1. Fabrication and characterization of magnetic responsive HAp-based RBCs

There is no characteristic group on the surface of superparamagnetic

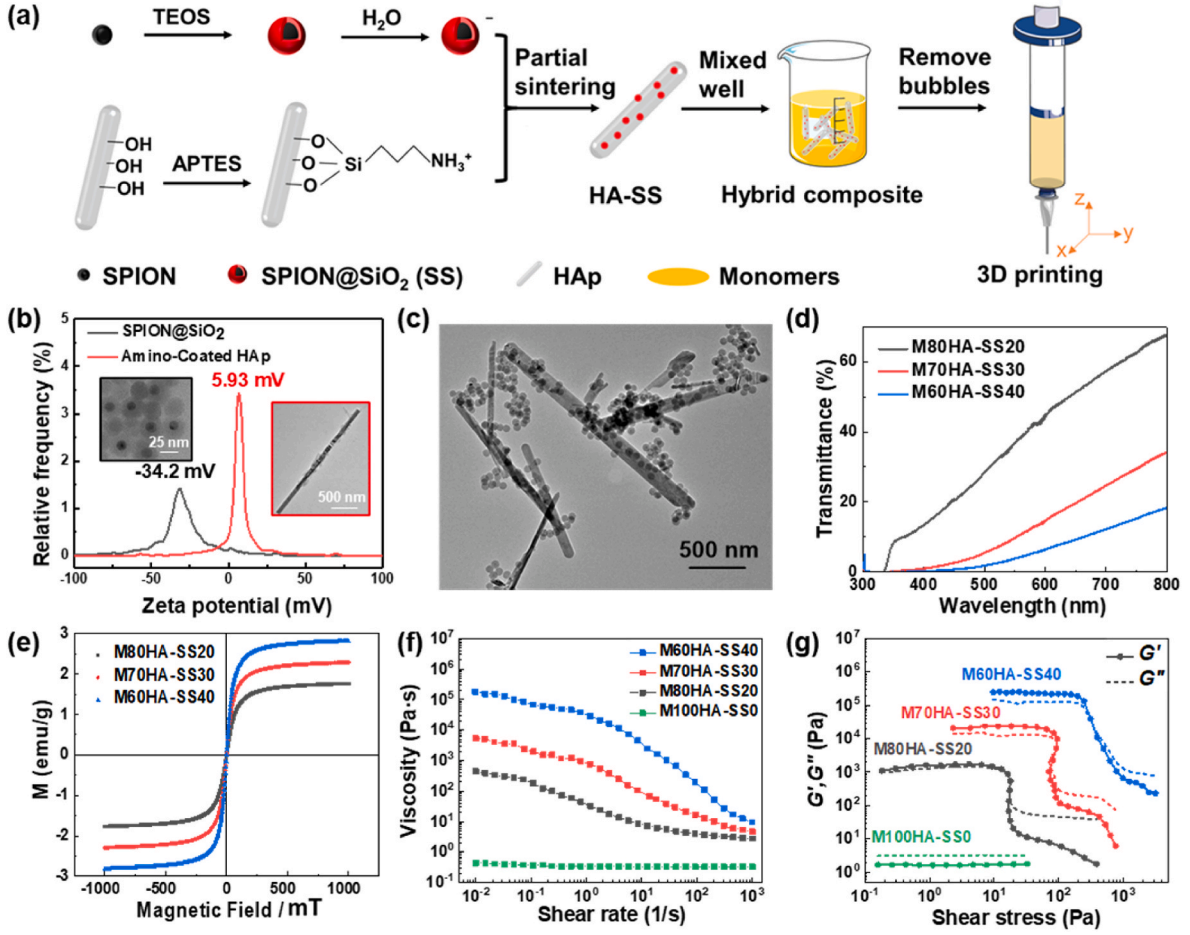

Fig. 1. Preparation and properties of magnetic responsive HAp-based RBCs inks. (a) Diagrammatic representation of the steps involved in preparing magnetic responsive HAp-based RBCs inks. (b) Zeta potential diagram of SS and amino-coated HAp in deionized water. Insets in the diagram represent the TEM images of SS and amino-coated Hap, respectively. (c) TEM image of HA-SS. (d) UV transmittance and (e) magnetic field-related hysteresis loop of RBCs filled with HA-SS with different contents. Rheological data were acquired for HA-SS RBCs inks formulated with M100HA-SS0, M80HA-SS20, M70HA-SS30, and M60HA-SS40 under two distinct conditions: (f) steady-shear and (g) oscillatory. The continuous curves illustrate the storage modulus G', whereas the dotted curves indicate loss modulus G''.

iron oxide (SPION) nanoparticles integrated with the essential ingredient HAp of the tooth. Moreover, SPION cannot satisfy the esthetic requirements of dental restorations due to its black features. Therefore, the magnetized HAp nanorods were fabricated according to the process depicted in Fig. 1a. Firstly, monodispersed SPION@ SiO_2 (SS) particles were synthesized to coat SPION and add active groups according to the method in the literature [29]. The morphology and structure of SS were confirmed by TEM and the characteristic peaks of FT-IR spectra (Figs. S1a–c). Secondly, HAp rods were modified with amino silicone using the method reported by Wang et al. [30] The modified HAp nanorod has a rough surface and attachments (Figs. S1d–e). The characteristic peaks revealed that aminopropyltriethoxysilane (APTES) had been successfully grafted onto the surface of HAp nanorods (Fig. S1f). Finally, SS was introduced on HAp rods by electrostatic adsorption of oppositely charged particles and high-temperature sintering [31]. SS nanoparticles are negatively charged due to the formation of Si-O- groups on the surface in neutral deionized water, and modified HAp nanorods are positively charged amino silane groups, consistent with the Zeta potential test results (Fig. 1b). SS nanoparticles were dispersed randomly on the surface of HAp nanorods, as shown in Fig. 1c. High-temperature sintering followed by heat treatment facilitated stronger interactions between its surface and HAp, enhancing the adsorption effect and rendering the structure more stable. Images of HA-SS powders are shown in Fig. S2. Magnetized HA-SS-based RBC inks were prepared by mixing HA-SS powders into a resin matrix for further printing. They were labeled M100HA-SS0, M80HA-SS20, M70HA-SS30, and M60HA-SS40, respectively, representing a Bis-GMA/TEGDMA blend, with CQ and 4-EDMAB serving as photo initiators (M) and HA-SS mass fraction ratios.

HAp nanorods have a relatively high refractive index, and the photorefraction generated by the combination with SS nanoparticles further decreases the optical propagation. Incorporating HA-SS fillers significantly reduced the ultraviolet (UV) transmittance (Fig. 1d) and improved the magnetic response performance (Fig. 1e). When the filler content was 30 wt%, the UV transmittance was 54.24 %, and the saturation magnetization was 1.76 emu/g. Incorporating HA-SS fillers also improved the rheological properties for printing, converting the Newtonian fluid to a viscoelastic substance characterized by a clear yield point (Fig. 1f and g). HA-SS-based inks with high viscosity are conducive to maintaining the shape of the line after extrusion, thereby keeping a

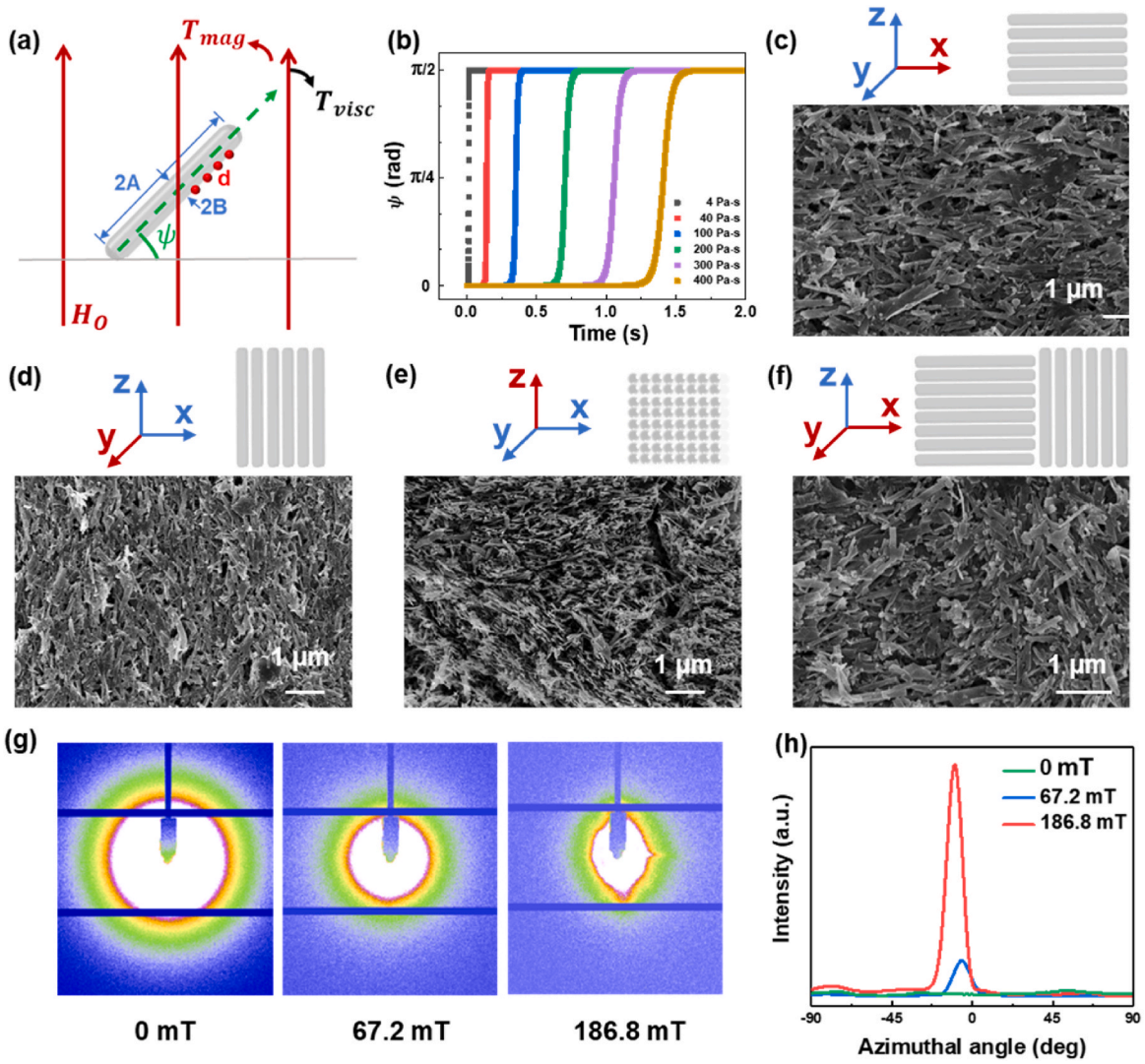

Fig. 2. The micro-structured architectures of HAp nanorods can be direction-controlled with 3D magnetic printing. (a) Schematic representation of an HAp nanorod undergoing alignment with an out-of-plane magnetic field, *Ho*. (b) Theoretical prediction for the evolution of an HAp nanorod angle over time in RBCs with a viscosity of 4, 40, 100, 200, 300, and 400 Pa s. The arrangement direction and corresponding surface SEM micrograph of HAp nanorods under the magnetic field of (c) x-axis, (d) y-axis, (e) z-axis, and (f) perpendicular to each other. The red arrow represents the direction of *Ho*. μSAXS patterns at locations with magnetic field intensities of (g) 0 mT, 67.2 mT, and 186.8 mT and (h) its corresponding azimuthal scan. M70HA-SS30 inks were used in the experiments.

stable structure. As shown in Fig. 1g, the inks were in a solid-like state ($G'>G''$) under the initial shear stress. When approaching the yield stress ($G' = G''$), the modulus decreased sharply, resulting in viscous deformation ($G'<G''$). This change was beneficial to the extrusion of ink from the printing nozzle under the action of external force and the recovery of its solid-like characteristics after leaving, which were crucial to prevent distortion of printed objects. Three-interval thixotropy test also verified the capacity of inks to recover rapidly after extrusion (Fig. S3), indicating the ideal suitability of these inks for 3D printing. The addition of HA-SS nanoparticles to RBCs ink improved the printability and forming precision of the ink (Fig. S4).

2.2. Magnetically induced orientation of HAp-based RBCs

The alignment duration of magnetized particles is influenced by solution viscosity, the magnetic field strength, nanoparticle coverage, and the relationship between the direction of the magnetic field and the base level (parallel or perpendicular) [32]. When a magnetic field is applied, HAp nanorods need to overcome the viscous torque under the action of magnetic torque that works to align the long axis with the field direction (Fig. 2a). Numerical solutions of this second-order differential equation were used to estimate the time required for orientation during the printing process according to the equation in the literature [33,34]. The concrete analysis is presented in the Supplementary Information Discussion. The alignment time for an applied magnetic field of 100 mT in M70HA-SS30 inks (η~400 Pa s) extruded during nozzle is ~1.6 s, as shown in Fig. 2b.

To demonstrate the capability of HAp closely arranged in an orderly manner along the magnetic field direction, we created choice reinforcement architectures in different directions and specific regions (Figs. 2c–f and Figs. S5–6). The specific orientation of reinforcement architecture is shown in the simplified microstructures, which is believed to contribute to the outstanding properties. The initial 2D SAXS patterns of samples induced by a magnetic field of 186.8 mT showed higher anisotropy (Fig. 2g) and a sharp peak near 0° in the azimuthal scan (Fig. 2h), indicating oriented arrangement of HAp nanorods. These patterns directly reflect the arrangement and orientation of HAp in the samples. With the increase in magnetic field intensity, significant changes in the scattering patterns can be observed, and the intensity distribution in the azimuthal direction of the SAXS pattern becomes narrower with higher anisotropy, demonstrating the high-order arrangement of HAp nanorods. The gradual increase in the magnetic field force resulted in an increased order parameter from 0.19 to 0.61 when the magnetic field increased from 0 mT to 186.8 mT. The SEM images in Fig. S5 provide microstructural information of HAp with increasing magnetic field intensity, serving as supplementary evidence. This change is mutually corroborated with the μSAXS results, jointly supporting the conclusion that the magnetic field has a significant impact on the orientation of HAp grains. These microstructures were imported into our 3D magnetic printing framework to recreate composites with bioinspired tooth microstructural design.

2.3. Mechanical properties of 3D-printed RBCs

At the DEJ, the nanoscale structures of tooth are aligned in a nearly orthogonal configuration. This configuration effectively enhances tooth's toughness that improves its resistance to be damaged by disrupting crack extension and causing fractures to divert and distort [35]. To replicate the primary strengthening strategies that confer exceptional fracture durability, a magnetic field in different directions (the magnetic

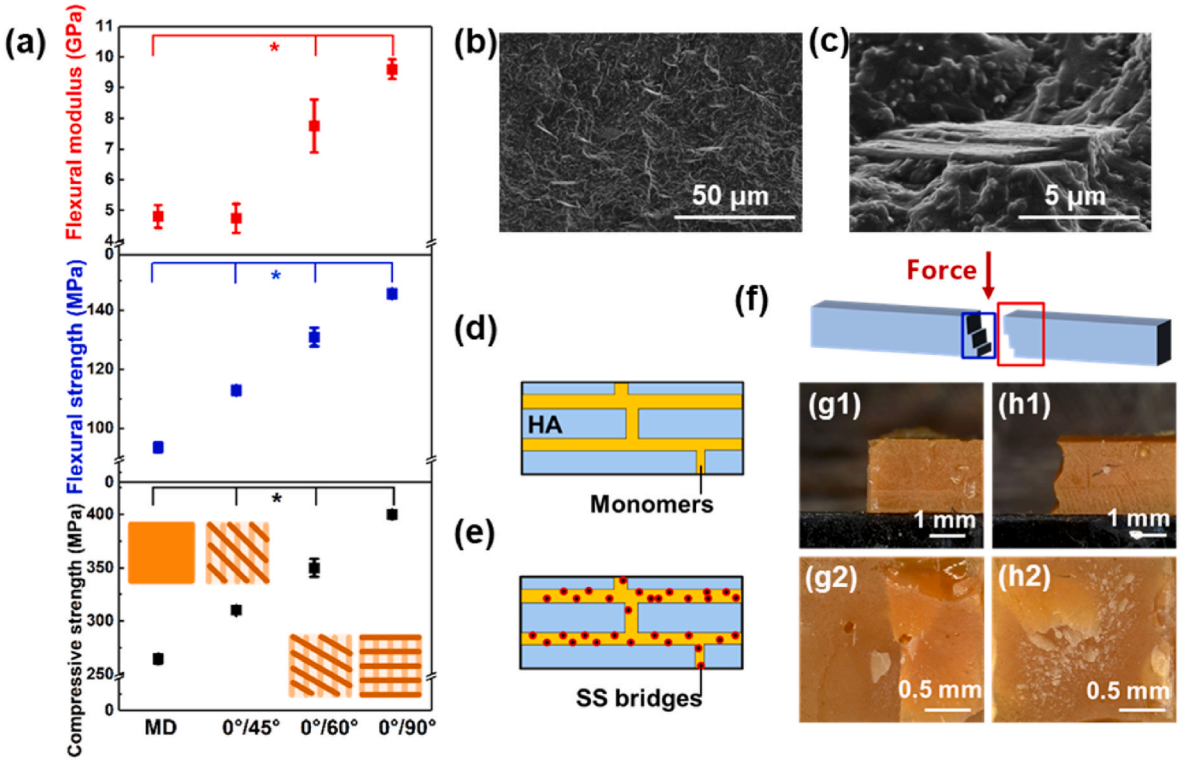

Fig. 3. Mechanical properties of 3D-printed RBCs. (a) S_F, E_Y, and S_C of the specimens fabricated via MD and 3D printing with distinct print paths. *p < 0.05 signifies a statistically meaningful distinction when contrasted with MD method. The orange diagram in the compressive strength graph illustrates the design schematic of the orientation direction of the HA-SS nanorods, encompassing both the molding method and the distinct internal architectures. The cross-sectional SEM images of (b–c) 3D printing. (c) An enlarged view of (b). Schematic of (d) pure HAp nanorods and (e) HAp nanorods coated with SS nanoparticles highly ordered to enhance RBCs samples. (f) Schematic of the fracture under force. Morphology observed from a lateral perspective of specimens manufactured through (g1) MD and (h1) 3D printing, as indicated in the red box in (f). Cross-sectional images of cured cuboids fabricated using (g2) MD and (h2) 3D printing following a three-point flexure analysis, as indicated in the blue box in (f).

field direction is along the printed line) was configured in the adjacent layer of the printed spline to arrange HAp nanorods.

Flexural modulus (E_Y), flexural strength (S_F), and compressive strength (S_C) of the magnetized HAp-based RBCs were quantified to assess the enhancement impact. The data is shown in Fig. 3a and Fig. S7. The splines with the highly orientated HA-SS nanorods exhibited better mechanical strength than the molding method (MD). In the 3D-printed M70HA-SS30 with 0°–90° orientation, the highest E_Y, S_F, and S_C values were 9.6 ± 0.3 GPa, 145.6 ± 1.6 MPa, and 400 ± 4.0 MPa, respectively. Some studies have reported similar results on the effect of orientation direction on mechanical properties [36]. It can be clearly seen that the S_F of HA-SS-based RBCs is superior to most commercial resins and is compatible with human dentin (Fig. S8). The compatibility helps prevent premature failure in both tooth replacements and natural teeth, as it ensures stress levels are well-matched. SEM images showed that the internal cross-section of the 3D-printed sample had more fractures than the molded sample after the three-point bending test (Figs. S9a–b). Additionally, a stepped surface was formed by plenty of highly ordered HAp nanorods in the cross-section of the 3D-M70HA-SS30 sample with an orientation of 0–90° (Fig. 3b). Small SS particles with a certain surface roughness were observed on the stepped surface after magnification (Fig. 3c). Different from the "brick-wall" mechanism of pure Hap and sequentially reinforced RBCs (Fig. 3d), HA-SS nanoparticles resemble a "brick-bridge" structure due to loading SS particles on the surface of HAp nanorods (Fig. 3e). As described in the literature [37], the vertical interfaces prevent crack propagation, and the interlocking of nano-protrusions withstands greater stress before failure. The interruption and deflection of crack propagation (Figs. 3f–h) possibly enhance this structure's mechanical properties, similar to the strengthening mechanism of natural teeth.

2.4. Individual 3D-printed dental crown with multi-materials

HAp nanorods were controllably and highly aligned in RBCs induced by shear force and external magnetic field. To simulate the difference in tooth composition of the components, two materials were further used to print dentin and enamel, respectively. Firstly, the dental model with each printed layer was separated into two groups regarding different reinforced orientations in enamel and dentin. Secondly, M70HA30 was induced to arrange into dentin by shear force as shown in gray direction (Fig. 4a, S10a). After completion, a UV light was used to polymerize this area, consolidating the structure and fixing the orientation of reinforcement. Thirdly, M70HA-SS30, with improved mechanical strength and controllable structure, was induced as enamel vertical order in a specific magnetic field (Fig. 4b, S10b) using a dual-nozzle device by a 3D printer. These active parts were then UV-polymerized. The above steps

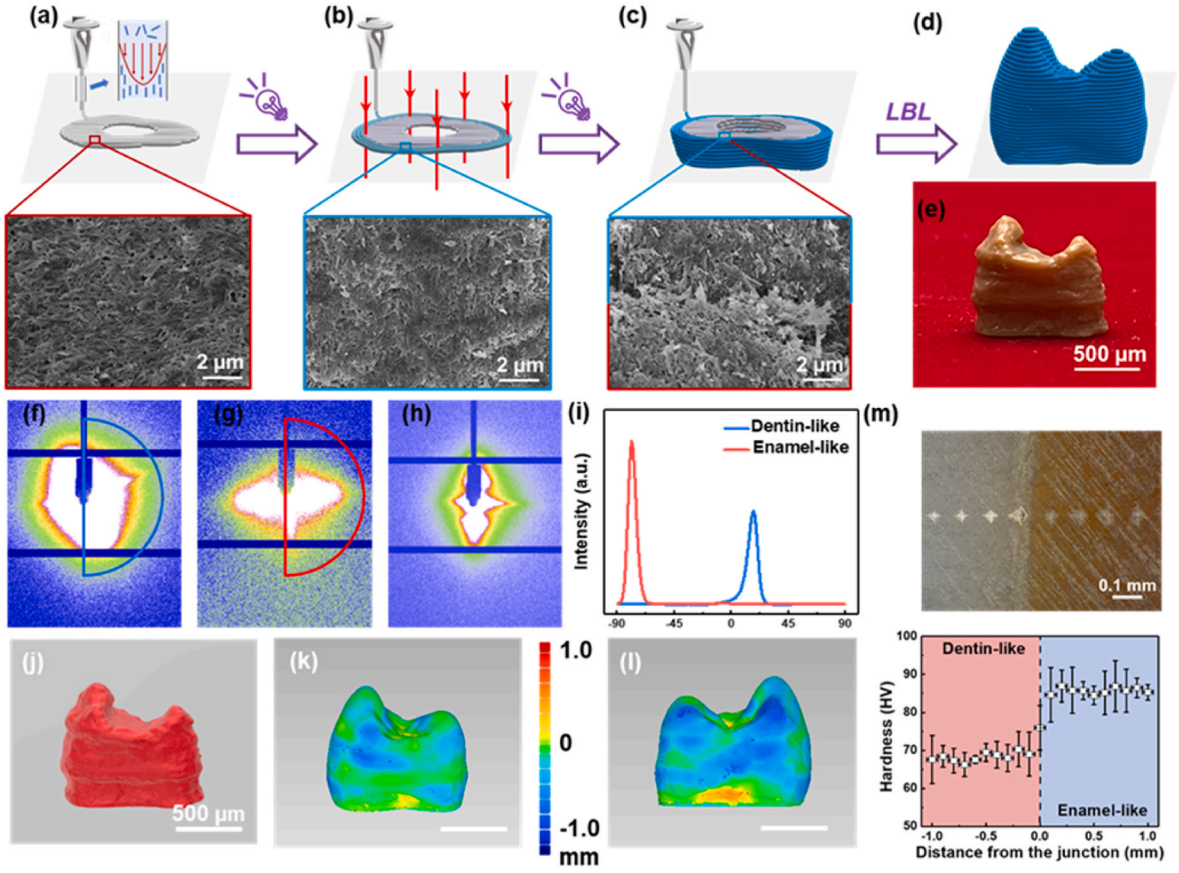

Fig. 4. Tooth structure prepared by HAp-based multi-material RBCs inks. Schematic representation of (a) the dentin structure printed by M70HA30 induced by shear force and the nanorods aligned along the printing path, (b) the enamel structure printed by M70HA-SS30 induced by a magnetic field and the nanorods aligned along the magnetic field, (c) semi-manufactured dental crown, (d) the final 3D model of the canine crown and its corresponding SEM image. The lamp, red arrow line, "*LBL*" representing the UV curing process, the direction of the magnetic field, and layer-by-layer printing, respectively. (e) The photography of a 3D-printed canine crown with multi-materials. SAXS patterns at (f) dentin-like parts, (g) enamel-like parts, (h) DEJ, and (i) azimuthal scan. The integral region is shown as the semicircle in the figure, from −90° to 90°. (j) A 3D model of a polished canine tooth, captured using micro-CT. Deviation map (mm) comparing the morphological structure of the front (k) and back (l) surface between the digital 3D representation of natural canine and the refined, 3D-printed canine replica. The color-coded mapping serves to visualize the variations, where the positive value highlights instances where the dimensions of the 3D-printed model exceed the original, while negative values indicate the opposite. Scale bar: 0.5 cm. (m) The micromorphology and hardness gradient achieved through the precise manipulation over the alignment and chemical constituents of local nanorods within the composite structure. Error bars represent standard deviation across three individual tests.

were repeated for each unique reinforcement orientation for final incorporation into the composite layer (Figs. 4c–d, S10c-d). The final printed crown is shown in Fig. 4e and S10e. In the corresponding SEM images, HAp nanorods in enamel and dentin were arranged vertically and parallel to the bottom of the crown, respectively. The DEJ also had the same morphological characteristics. The above 3D printing process also synchronously realized the layered structure of the tooth. Firstly, the HAp nanoparticles (nanoscale) responded to the shear force or external magnetic field and were oriented to form a tightly arranged structure (micron scale). Then the HAp nanorods were arranged perpendicular to each other in different regions (millimeter scale), finally forming a complex macroscopic tooth composite structure (centimeter level). The 2D SAXS patterns showed orientation characteristics in different directions at specific parts (Figs. 4f–h). The direction of its azimuth was different, indicating that the direction of its orientation was inconsistent. The azimuthal distributions of dentin-like and enamel-like were almost perpendicular to each other, considering that the peak position angle difference was about 90° (Fig. 4i).

To demonstrate the versatility of structure control, illustrative examples of canine, incisor, and molar tooth crown structures were fabricated, as depicted in Fig. S11. The 3D-printed crown exhibited layering artifacts arising from the constraints in slicing accuracy. Subsequently, the surface of the canine crown was refined through polishing to mimic an essential aspect of the clinical restoration process, and Fig. 4j showcases a detailed 3D rendering of its counterpart. The sleekly polished canine crown formations possessed smoothly contoured edges, rendering them well-suited for dental therapeutic applications. The discrepancy map illustrating the morphological variations on both the anterior (Fig. 4k) and posterior (Fig. 4l) surfaces exhibited a standard deviation value of ±0.1558 mm, as depicted in the histogram presented in Fig. S12. Furthermore, the achieved alignment precision reached an impressive 97.9 % based on the crown model.

To investigate the impact of unique location-dependent variations in texture and density within the enamel and dentin layer on the localized mechanical characteristics of the composite material which is inherently heterogeneous in nature, we conducted microhardness tests specifically targeting the transitional zone between the enamel-like and dentin-like parts. Analogous to the dentinoenamel junction observed in real tooth, our observations reveal that the peak in local hardness occurs at the outermost surface, gradually diminishing across the bilayer interface, and ultimately settling into a lower, steady-state value deep within the dentin-like interior. (Fig. 4m). The synthetic DEJ exhibited a gradual transition approximately 100 μm in length, attributable to an alteration in the arrangement and concentration of the nanorods of the boundary between the two layers. The correlation is strengthened by the robust association between the local hardness, the abundance of silica and the alignment of the nanorods.

2.5. Biological activity in vitro of 3D-printed multi-material RBCs

Excellent bioactivity can reduce adverse reactions between materials and biological tissues, mitigate inflammation, and enhance tissue integration, ultimately leading to better patient outcomes. Human dental pulp stem cells (HDPSCs) have broad application prospects in reconstructing and treating dental and oral tissue defects [38]. The concrete analysis of the appropriate cytotoxicity of printed dental crown culture dish is shown in the Supplementary Information Discussion (Figs. S13–15).

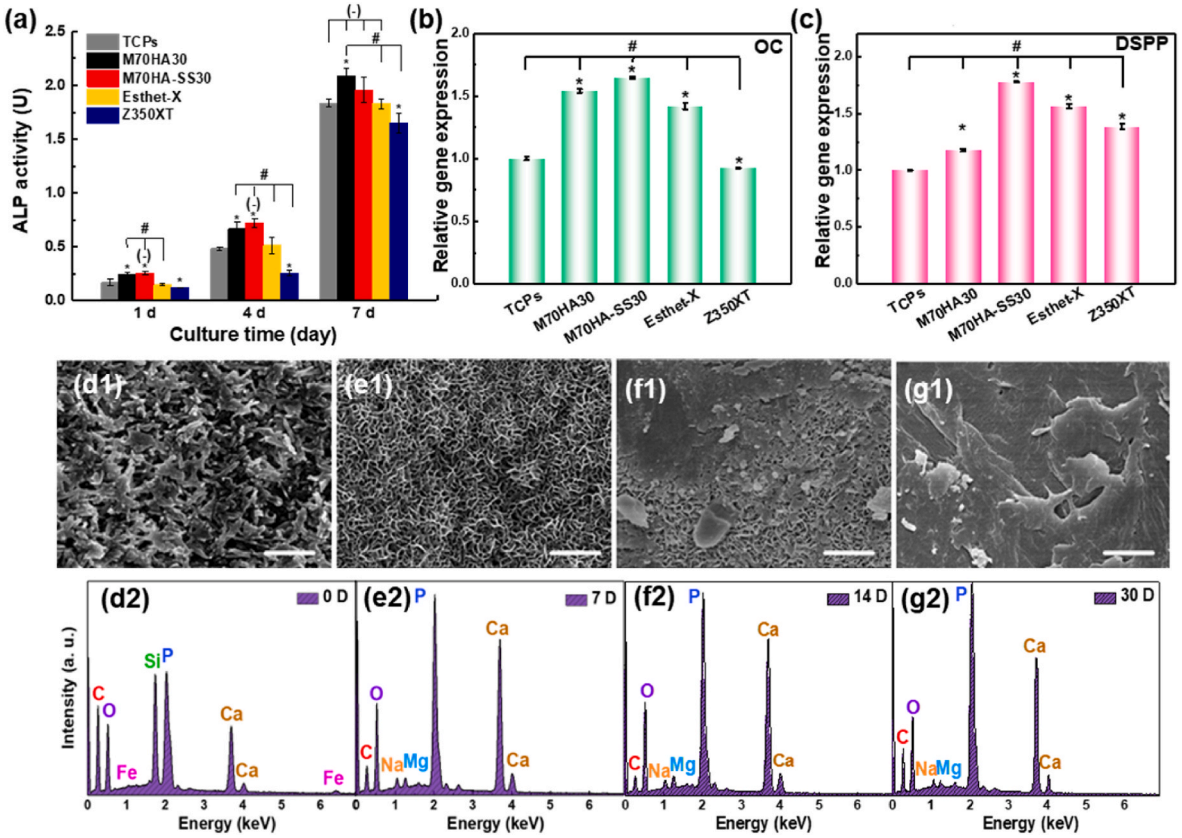

Fig. 5. Osteogenic differentiation and *in vitro* biological activity of 3D-printed multi-material RBCs. (a) The ALP activity expression of HDPLSCs cultured on coverslips (negative control) and the M70HA30, M70HA-SS30, Esthet-X, and Z350XT for 1, 4, 7 days. The relative expression of osteogenic characteristic genes (b) OC and (c) DSPP of HDPLSCs cultured for 21 days, where $*p < 0.01$ means in contrast to coverslips; $\#p < 0.01$ means in comparison to Esthet-X; (−) $p > 0.01$ means compared with M70HA30. FE-SEM images (d1-g1) and EDS profiles (d2-g2) of the surface composition of M70HA-SS30 following immersion in SBF for (d) zero day, (e) one day, (f) fourteen days, and (g) thirty days.

The intracellular alkaline phosphatase (ALP) is a cell marker of osteogenic mineralization of dentin and bone tissue. According to Fig. 5a, M70HA30 had better osteogenic differentiation performance than other materials, and M70HA-SS30 was better than Z350XT ($p < 0.01$) and comparable to Esthet-X and TCPs ($p > 0.01$) after seven days. M70HA30 and M70HA-SS30 contain excellent bioactive HAp fillers that promote cell differentiation, while Esthet-X contains bioactive barium aluminum fluoroboric acid silica glass components. The protein Osteocalcin (OC) secreted by osteoblasts at the late stage and the expression of Dentin matrix protein-1 (DMP-1) and Dentin sialo phosphoprotein (DSPP) in the last stage of odontogenic differentiation were significantly up-regulated in M70HA-SS30 than in other materials (Fig. 5b, c, Fig. S16). Doping silicon in M70HA-SS can improve the solubility of HAp in the medium, facilitating the generation of type I collagen and the differentiation of osteoblasts *in vivo* and *in vitro* [39]. As mentioned above, calcium and phosphorus in M70HA-SS30 and M70HA30 positively affected cell differentiation. Alizarin red staining (Fig. S17) showed that M70HA30 and M70HA-SS30 induced bone significantly, promoted the differentiation of HDPSCs to osteoblasts, and formed a mineralized matrix.

In the simulated body fluid environment, the material induced the ions to form a mineralized layer of inorganic salts on the material surface through the bioactive components. It can be observed that compared with the sample before being soaked (Fig. 5d1), the surface of M70HA-SS30 was covered by a porous flaky mineralized layer after seven days (Fig. 5e1). After 14 and 30 days of immersion, the surface of RBCs was spread with a dense, substantial layer (Figs. 5f1-g1), exhibiting a characteristic mineralized layer morphology with seamless lamination, further illustrating that the loading of SS nanoparticles did not affect the remineralization bioactivity of HAp nanorods. The EDS analysis results revealed that primary elements present in the surface material were carbon, oxygen, calcium, and phosphorus (Figs. 5d2-g2). The map of the mineralized layer showed a large amount of calcium and phosphorus after soaking, possibly originating from the deposited apatite coating. The above results prove that HA-SS-based RBCs exhibited excellent remineralization biological activity *in vitro*, promoting a closer and stronger bond between composite resin and teeth and further reducing microleakage.

3. Conclusions

A tooth crown with multiple ordered hierarchical structures was constructed by multi-materials, which could promote the proliferation, adhesion, and osteogenic differentiation of HDPSCs. This bionic study demonstrated that 3D magnetic printing offers a superior and rapid additive manufacturing technique for fabricating tailored hierarchical composites. This technique enables precise designing of the intricate microstructural characteristics and constituent makeup of complicated composites within intensely mineral-rich setups, thereby broadening the intentional landscape for creating bio-mimetic materials. This affords an opening for incorporating distinctive design principles arising from the evolution of biomaterials into synthetic composites and eventually developing an extensive array of functional biologically inspired material systems that remain inaccessibility through conventional technologies. This technology, designed for biomedical applications, can be extended to additional fields, such as the bone-cartilage interface and tendon-bone interface, to further verify its universal applicability and establish its superiority.

4. Materials and methods

4.1. Materials

Laboratory-grade ammonium hydroxide, urea, calcium nitrate tetrahydrate, ammonium hydrogen phosphate, methanol and ethanol were procured from Sinopharm Chemical Reagent Beijing Co. Ltd. 2,2-bis[4-(2-hydroxy-3-methacryloyloxy propoxy)phenyl] propane (Bis-GMA), triethylene glycol dimethacrylate (TEGDMA), n-hexane and Igepal CO-520 were all sourced from Sigma-Aldrich. Additionally, camphorquinone (CQ, 97 %) and ethyl-4-dimethylaminobenzoate (4-EDMAB, 99 %) were obtained from J & K Scientific. Meanwhile, propylamine and cyclohexane solvents were acquired from Sinopharm Chemical Reagent Co., Ltd. SPION was purchased from Japan Magnetic Fluid Technology Co., Ltd. γ- APTES was purchased from Macklin Biochemical Technology Co., Ltd. HDPSCs were purchased from Shanghai Yiyan Biotechnology Co., Ltd. DMEM F12 medium and Imported GIBCO fetal bovine serum (FBS) were sourced from Gibco, USA. Human related stem cells osteogenic differentiation complete medium and Alizarin Red Staining Solution were purchased from Guangzhou Saiye Biotechnology Co., Ltd. ALP detection box was supplied from Beyotime Biotechnology Co., Ltd. Triton X-100 Cracking Solutions was purchased from Thermo Fisher Technology Co., Ltd. MagneSil Total RNA mini-Isolation System was obtained from Promega, USA. Specific PCR primers was purchased from Shanghai Daixuan Biotechnology Co., Ltd. NdFeB Permanent was purchased from Magnet Ningbo Magnetic Abao Technology Co., Ltd. Dentition model (BZ-KQ059) was obtained from Bai Zhou Science Equipment Co., Ltd. Simulated Body Fluid (SBF) was bought from Phygene Life Sciences Co., Ltd.

4.2. Preparation of magnetic HAp nanorods

The synthesis of HAp nanorods involved a combined approach utilizing the high-gravity precipitation method with an RPB reactor, followed by hydrothermal treatment, as described in our previous report [40]. Firstly, monodisperse SPION@SiO_2 (SS) was synthesized by encapsulating SPION nanoparticles with an alkali-catalyzed silica layer formed by TEOS in an oil-in-water inverse microemulsion system [41]. The injection rate was 1.0 mL/h and the reaction time was 24 h. The synthesized HAp nanorods were subsequently silanized using APTES, following a previously established method [30]. SS nanoparticles were finally introduced on the HAp nanorods using electrostatic adsorption of oppositely charged particles and high temperature sintering, which is labeled as HA-SS [31]. SS and aminated HAp were dispersed in deionized water at concentrations of 1 g/80 mL and 1 g/30 mL, respectively, and sonicated for 10 min with a pulse/pause ratio of 0.6 to obtain SS and HAp suspensions. The two dispersions were then mixed and stirred for 2 days to complete the adsorption process. The powder particles were collected by vacuum filtration, washed sequentially with water and ethanol, and dried. Subsequently, the powder was sintered at 700 °C for 2 h (heating rate of 1.7 °C/min up to 400 °C, followed by maximum power to reach the peak temperature). Finally, the powder was dispersed in deionized water and absolute ethanol, collected by vacuum filtration through a 20 mm sieve, and vacuum-dried to obtain HA-SS powder.

4.3. Preparation of magnetic responsive HAp-based RBCs pastes

The silanized HA-SS (3 g) was uniformly mixed in 97 g of ethanol solution and subjected to ultrasonic agitation for 5 min to ensure thorough mixing and dispersion. The resin matrix comprised a Bis-GMA/TEGDMA blend (59.4/39.6, wt./wt.), with CQ (0.02 wt%) and 4-EDMAB (0.08 wt%) serving as photo initiators. Bis-GMA and TEGDMA were meticulously mixed until a uniform consistency was achieved. Subsequently, the photoinitiated blend was incorporated and vigorously stirred for 24 h to ensure complete homogeneity. The prepared resin matrix was incorporated into HA-SS ethanolic suspension, resulting in a combined mixture. Ethanol was removed by a rotavapor operating at a pressure-temperature condition of 30 bar and 80 °C, respectively, resulting in the formation of a concentrated ink composed of 30 wt% HA-SS which was designated as M70HA-SS30. The obtained ink was then subjected for mixing in a speed mixer (DAC 150.1 FVZ-K, FlackTek, Inc., Germany) at 2000 rpm for 5 min to ensure thorough

homogenization and blending of the ink components. All of the unprocessed inks were kept under a vacuum condition for a duration of 8 h to eliminate any trapped air bubbles, followed by storage in a fridge maintained at 4 °C). The manufacturing procedure of HA-SS based RBCs inks is depicted in Fig. 1a.

4.4. 3D printing of magnetic RBCs inks based on HA-SS

Syringes containing HA-SS based RBCs pastes were installed in the BioScaffolder Printer 4.2 (Gesim, Germany). Pastes were propelled through micro-sized nozzles with an inner diameter (410 μm). The RBC inks were dispensed onto a glass slide under pressures varying between 100 and 600 kPa, while maintaining a speed of 1–8 mm/s. A stable and uniform magnetic field is generated by a cuboid permanent magnet, and the size and direction of the magnetic field are regulated by physical rotation and translation. The magnitude of its magnetic field varies with the distance, as shown in Fig. S18. Subsequent curing procedures and molding method were conducted in accordance with our previous work [4].

Apart from tooth crowns, various CAD (computer-aided design) specific shapes including rectangle (25 × 2 × 2 mm) and cylinder (Φ 4 × 6 mm, Φ 10 × 1 mm, Φ 1 × 10 mm) were fabricated for conducting three-point bending tests, compressive tests, hardness assessments, biocompatibility measurements, and *in vitro* bioactivity tests, respectively.

The tooth 3D model was scanned and digitally recreated using a micro-CT scanner (InspeXio SMX-225CT FPD, Shimadzu, Japan). Each printed layer was preliminarily cured, and ultimately, multi-materials RBCs inks based on HAp were fully cured to form a complete tooth structure.

4.5. Characterization of nanoparticles

The surface morphology was characterized using a transmission electron microscope (TEM, JEOL JEM-2100F, Japan) by an accelerating voltage of 200 kV. The potential of SS and aminated HAp was analyzed by Zeta potential analyzer (Anton Paar Litersizer500).

4.6. Performance of magnetic HAp-based inks

The optical properties were analyzed by ultraviolet–visible spectrometer (Shimadzu UV3600). The saturation magnetization was measured by Vibrating Sample Magnetometer (VSM, Quantum PPMS-9). Rheological tests were conducted by a HAAKE RS150L rheometer (Thermo Fisher Electron Co., Germany) equipped with a 2 cm plate-plate geometry (gap = 300 μm). The steady shear viscosity was determined at various shear rates ranging from 0.01 to 1000 s^{-1} conducted at 37 °C. Storage and loss modulus were derived from stress-controlled oscillatory tests conducted at a frequency of 1 Hz at room temperature. The yield stress of the various paste was determined as the intersection point between *G'* and *G"*.

4.7. Characterization of samples

The specimens' surface topography was examined using a scanning electron microscope (SEM, Hitachi S-4800) operated at a voltage of 10 kV. The degree of order is calculated according to the proportion of HAp nanorods arranged along the magnetic field direction in the SEM images. S_F, E_Y, and S_C were quantified using an electronic universal material tester(Instron 5900, USA), in accordance with established literature procedure [42]. The testing parameters of samples were tailored to align with ISO 4049-2019 standards. Rectangular samples (n = 6) were used for the three-point fracture test with a spacing distance of 2 cm, a cross-member speed of 0.0125 mm/s. On the other hand, cylinder-shaped specimens (n = 6) were prepared for the compressive test, conducted at a loading speed of 10 cm/min. The specimens underwent polished with 2500-grit sandpaper prior to the test. Hardness was quantified along a line traversing the interface between the enamel-like and dentin-like layers using a micro-Vickers hardness tester (HXD-1000TMC/LCD, manufactured by Shanghai Taiming Optical Instrument Co., Ltd.). The indenter load is 200 GF and the load duration is 40 s. Indentations were performed at intervals of 100 μm, starting from inner layer towards outer layer of biomimetic teeth.

4.8. Synchrotron radiation small-angle X-ray scattering

The orientation of HAp-based RBCs was examined using SR-SAXS, conducted on the BL19U2 station located at the Shanghai Synchrotron Radiation Facility. The beam spot size measured 50 × 450 μm^2, the selected X-ray wavelength (λ) was 0.104 nm, while the distance between the sample and detector was maintained at 2680 mm with an exposure time of 1 s. The tooth-like slice was imaged using a micro-focused X-ray beam as depicted in Fig. S19 shown. The detailed testing procedures and calculation methods of the order parameter are outlined in the published literature [43]. Azimuth integral ranges from −90° to 90°.

4.9. Manufacturing of a tooth crown model utilizing 3D printing

The printed dental crown was refined by hand using an electric polisher and abrasive compound to achieve a smooth finish. Then the refined crown underwent another imaging using Micro-CT for further analysis. The three-dimensional graphics congruency between the refined models and their corresponding actual models was thoroughly assessed, forming the criterion for evaluation. Geomagic Qualify 2013 software (Raindrop Geomagic Company, USA) was utilized to achieve a precise, individual matching process between the refined 3D crown model and its original counterpart. After analyzing the distribution color map, we can accurately assess the extent of the difference.

4.10. Osteogenic differentiation

The degree of increase in alkaline phosphatase activity as a qualitative and quantitative indicator of stem cell differentiation. When HDPSCs were cultured in osteogenic induction medium for 1d, 4d and 7d, the mineralization induction medium was discarded and gently rinsed with PBS. Then 100 μL 1 % Triton X-100 was employed to lyse the cells for 30 min, fand then incubated at 37 °C for 15 min. The test solution was added according to the ALP detection kit instructions, and multi-function microplate reader detected its absorbance at 405 nm wavelength. RT-PCR test and alizarin red staining as shown in Supplementary Information Experimental.

4.11. In vitro biological activity

The capacity of the HA-SS derived RBCs to form apatite was assessed in SBF, employing a method akin to those previously described [44]. In summary, disc-shaped specimens measuring Φ10 mm × 1 mm were submerged in 20 mL SBF maintained at 37 °C for duration of 1, 14 and 30 days, and the SBF was refreshed weekly. Samples underwent a gentle rinsing process into deionized water, followed by a drying period at 60 °C for 6 h prior to testing. The changes of surface morphology and chemical constituency were analyzed using SEM integrated with an energy dispersive X-ray spectrometer (EDS, Quantax 400, Bruker, Germany).

4.12. Statistics analysis

Data of mechanical properties were presented as average ± SD derived from a minimum of three individual tests. Quantitative evaluation was conducted out with SPSS 25.0. One-way ANOVA was performed among all groups. Significance was established at a threshold of $p \leq 0.05$ across all scenarios.

CRediT authorship contribution statement

Menglu Zhao: Writing – review & editing, Writing – original draft, Methodology, Formal analysis, Data curation. **Yanan Geng:** Validation, Project administration. **Suna Fan:** Project administration, Funding acquisition. **Xiang Yao:** Resources, Methodology. **Jiexin Wang:** Resources, Formal analysis. **Meifang Zhu:** Resources, Project administration, Funding acquisition, Conceptualization. **Yaopeng Zhang:** Writing – review & editing, Supervision, Resources, Project administration, Methodology, Funding acquisition, Conceptualization.

Declaration of competing interest

The authors declare that they have no known competing financial interests or personal relationships that could have appeared to influence the work reported in this paper.

Acknowledgments

This work was sponsored by the National Key Research and Development Program of China (2016YFA0201702), the Natural Science Foundation of China (52173031), and the Natural Science Foundation of Shanghai (20ZR1402400). The authors thank Mr. Mianbo Ning (Shimadzu) for the help in micro-CT characterization.

Appendix A. Supplementary data

Supplementary data to this article can be found online at https://doi.org/10.1016/j.mtbio.2025.101454.

Data availability

Data will be made available on request.

References

[1] H. Deyhle, et al., Proc. SPIE 7401 (2009) 74010.
[2] V. Imbeni, et al., Nat. Mater. 4 (3) (2005) 229.
[3] H. Deyhle, et al., Acta Biomater. 10 (1) (2014) 355.
[4] M.L. Zhao, et al., Adv. Sci. 9 (5) (2022) 2104001.
[5] Y. Sun, et al., Adv. Mater. (2023) 2302824.
[6] H. Le Ferrand, et al., Nat. Mater. 14 (11) (2015) 1172.
[7] H.W. Zhao, et al., Science 375 (6580) (2022) 551.
[8] Revilla-Leon, M., et al., J. Prosthodontics (2018) 27 (6) 560.
[9] A.J. Cresswell-Boyes, et al., Sci. Rep. 12 (1) (2022) 7830.
[10] X. Yang, et al., Adv. Sci. 10 (5) (2023) 2205041.
[11] J. Yue, et al., Adv. Funct. Mater. 25 (43) (2016) 6756.
[12] J. Young Park, et al., J. Mater. Chem. B 3 (2015) 5415.
[13] B. Arsuffi, et al., Adv. Funct. Mater. (2024) 2409864 **n/a** (n/a).
[14] G. Siqueira, et al., Adv. Funct. Mater. 27 (12) (2017) 1604619.
[15] D. Kokkinis, et al., Nat. Commun. 6 (1) (2015) 8643.
[16] C. Pearson, et al., Mater. Today: Proc. 64 (2022) 1403.
[17] Z. Ma, et al., Adv. Funct. Mater. 34 (42) (2024) 2406108.
[18] W.C. Liu, et al., Nat. Commun. 13 (1) (2022) 5015.
[19] P. Agrawal, et al., Adv. Mater. 36 (40) (2024) 2408374.
[20] T. Ma, et al., Nat. Commun. 15 (1) (2024) 6317.
[21] Y. Yang, et al., Adv. Mater. 30 (36) (2018) 1706539.
[22] C. Zhu, et al., Adv. Mater. 36 (34) (2024) 2314204.
[23] C. Lei, et al., Adv. Mater. 36 (16) (2024) 2311659.
[24] H. Dong, et al., J. Biomed. Mater. Res. 112 (9) (2024) 1412.
[25] A.D. Loguercio, et al., Dent. Mater. 39 (12) (2023) 1159.
[26] X.Y. Ma, et al., Dent. Mater. 40 (9) (2024) 1378.
[27] H. Le Ferrand, et al., Acta Biomater. 173 (2024) 66.
[28] M. Yashaaswini, et al., BIOINSPIRED BIOMIMETIC AND NANOBIOMATERIALS, 2024.
[29] F. Chen, et al., Chem.-Asian J. 4 (12) (2009) 1809.
[30] L.Y. Wang, et al., Macromol. Mater. Eng. 305 (9) (2020) 2000188.
[31] T.P. Niebel, et al., J. Mech. Behav. Biomed. 60 (2016) 367.
[32] B. Elder, et al., Adv. Mater. 32 (17) (2020) 1907142.
[33] R.M. zheErb, et al., Soft Matter 15 (17) (2019) 3628.
[34] R.M. Erb, et al., Science 335 (6065) (2012) 199.
[35] W. Huang, et al., Adv. Mater. 31 (43) (2019) 1901561.
[36] S.R. Rajpurohit, H.K. Dave, Adv. Manuf. 6 (4) (2018) 430.
[37] R. Libanori, et al., Bioinspiration Biomimetics 11 (3) (2016) 036004.
[38] H. Liu, et al., ACS Appl. Mater. Interfaces 15 (28) (2023) 33480.
[39] M.Y. Shie, et al., Acta Biomater. 7 (6) (2011) 2604.
[40] B.-Y. Lv, et al., Ind. Eng. Chem. Res. 56 (11) (2017) 2976.
[41] H. Xu, et al., J. Am. Chem. Soc. 128 (49) (2006) 15582.
[42] R. Wang, et al., Mater. Sci. Eng. C 50 (2015) 266.
[43] L. Lu, et al., Chem. Eng. J. 405 (2021) 126793.
[44] F. Liu, et al., Mater. Sci. Eng. C 53 (2015) 150.